THE JOURNAL OF PHYSICAL CHEMISTRY C

Article

Cite This: J. Phys. Chem. C 2018, 122, 18751−18758

pubs.acs.org/JPCC

Förster Resonance Energy Transfer Distance Dependence from Upconverting Nanoparticles to Quantum Dots

Sonia Melle,*[,†] Oscar G. Calderón,[†] Marco Laurenti,[‡] Diego Mendez-Gonzalez,[‡] Ana Egatz-Gómez,[§] Enrique López-Cabarcos,[‡] E. Cabrera-Granado,[†] Elena Díaz,[∥] and Jorge Rubio-Retama*[,‡]

[†]Department of Optics, Complutense University of Madrid, E-28037 Madrid, Spain

[‡]Department of Chemistry in Pharmaceutical Sciences and [∥]GISC, Department of Materials Physics, Complutense University of Madrid, E-28040 Madrid, Spain

[§]Center for Applied Structural Discovery, Biodesign Institute, Arizona State University, Tempe, Arizona 85287, United States

Supporting Information

ABSTRACT: Förster resonant energy transfer (FRET) with upconverting nanoparticles (UCNPs) as donors and quantum dots (QDs) as acceptors has been regarded as a promising tool for biosensing applications. In this work, we use time-resolved luminescence spectroscopy to analyze the UCNP-to-QD FRET and we focus on the most relevant parameter of the FRET phenomenon, UCNP−QD distance. This distance is controlled by a nanometric silica shell around the UCNP surface. We theoretically reproduce the experimental results applying FRET theory to the distribution of emitting erbium ions in the UCNP. This simple model allows us to estimate the contribution of every erbium ion to the final FRET response and to explore different strategies to improve FRET efficiency.

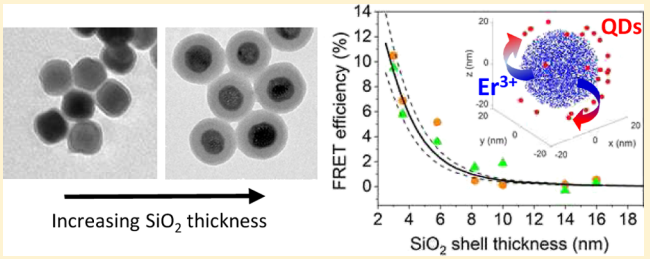

INTRODUCTION

Förster resonant energy transfer (FRET) is a physical process whereby the energy of a chromophore in the excited state (donor) can be transferred to a neighbor molecule that is in the ground state (acceptor), over a distance larger than the collisional radii. This phenomenon occurs when the donor and the acceptor are in close proximity, allowing the energy to be transferred without generation of any photons, through long-range dipole−dipole interactions.[1] The rate of the energy transfer depends on many different parameters, such as the extent of the spectral overlap between the emission spectrum of the donor and the absorption spectrum of the acceptor, the quantum yield of the donor, the relative orientation of the donor regarding the acceptor transition dipoles, and the distance between the donor and the acceptor.[2] The FRET's distance dependency has been crucial to detect two species in close proximity, enabling molecular rulers that can measure the distance between two specific molecules.[3] Such a feature in combination with the wide range of techniques for molecules and biomolecule functionalization with organic dyes has been applied to study the interaction between DNA, antigens, and proteins in vivo at the nanometer scale.[4]

During the last decades, advances in the synthesis of upconverting nanoparticles (UCNPs) with outstanding luminescence properties and higher photochemical stability than that of classical organic dyes have paved the way for analytical platforms using UCNP-based FRET systems.[5−12] Lanthanide-doped UCNPs are a special type of materials that are able to absorb low energy photons, typically in the near-infrared (NIR) wavelength, and emit UV−vis photons. Samples can be illuminated with high power densities of NIR light, with a high light penetration depth and without the risk of degradation or photobleaching, which is of especial interest for in vivo analyses.[12−15] Furthermore, the large anti-Stokes shift and the long lifetime allow us to separate the upconverting luminescence signal from biological sample autofluorescence, thus removing the background noise.[16] The narrow absorption and emission bands of UCNPs simplify the instrumentation for detecting and analyzing FRET processes.[17] However, the quantum efficiency in upconversion processes is rather low, and therefore, it is necessary to use an acceptor with high quantum yield and good spectral overlapping. Such requirements are fulfilled by quantum dots (QDs), which exhibit superb quantum yield and tunable absorption bands that can be adjusted to overlap with the emission band of the donor. Thus, the use of lanthanide-doped nanoparticles as donors and QDs as acceptors can be considered as ideal Förster pairs for bioassays.[18−21] Recently, Mattsson et al. have demonstrated a mix-and-measure UCNP-to-QD FRET system for rapid homogeneous bioassays for detecting analytes in aqueous solutions at nanomolar concentrations.[22]

A fundamental study of FRET between $NaYF_4$:Er^{3+}/Yb^{3+} nanoparticles and CdSe QDs was reported by Bednarkiewicz et

Received: May 23, 2018
Revised: July 4, 2018
Published: July 10, 2018

DOI: 10.1021/acs.jpcc.8b04908
J. Phys. Chem. C 2018, 122, 18751−18758

al.[23] They observed an Er^{3+} upconversion luminescence lifetime decrease from 153 to 130 μs because of the presence of QDs. These authors suggested two strategies to increase FRET efficiency: (1) diminishing the size of the UCNPs and (2) distributing the lanthanide active ions only in the outer shell of a core/shell UCNP. In this context, Murh et al. have recently analyzed the efficiency of FRET from UCNPs to organic dyes for UCNPs of different sizes.[24] As the UCNP size decreases, two competing phenomena take place. On the one hand, an increasing percentage of the UCNP Er^{3+} ions becomes involved in FRET, increasing its efficiency. However, on the other hand, the surface-to-volume ratio increase leads to more luminescence quenching at the UCNP surface, which reduces FRET strength. They indeed found a maximum FRET efficiency for a 21 nm-sized UCNP. In addition, Bhuckory et al. have analyzed the efficiency of FRET between Er^{3+} ions distributed over either the core or the shell of UCNPs and Cy3.5 dye acceptors.[25] The authors use the FRET efficiency results to estimate parameters such as donor−acceptor (DA) distances and Er^{3+} donor quantum yields. Very recently, Marin et al.[26] have experimentally demonstrated enhanced FRET from $LiYF_4:Yb^{3+},Tm^{3+}$ UCNPs to $CuInS_2$ QDs by following two strategies: reducing the size of the UCNPs and doping the lanthanide active ions in the outer shell of a core/shell particle.

Despite these interesting works in UCNP-based FRET systems, to the best of our knowledge, no exhaustive studies of the FRET efficiency dependence on distance have been carried out. These systems are rather complex because the potential donors are distributed inside the UCNPs, which sizes are comparable to the length scale of FRET. This leads to a distribution of DA distances, a crucial key to the energy transfer phenomena. In this work, we present an in-deep study of the distance dependence of FRET in UCNP−QD systems with the aim of developing more efficient UCNP−QD FRET biosensors. To control the UCNP−QD distance, we cover the UCNPs with a nanometric silica shell. By varying the shell thickness, we analyze the change of the upconversion luminescence lifetime and, therefore, the FRET efficiency. Upconversion process involves many transitions and competing mechanisms, which makes it very difficult to isolate the real contribution of FRET to the energy transfer process. Here, we assume that energy transfer is most probably due to FRET. Then, the experimental results are interpreted by using FRET theory and taking into account the multiple distances between individual donor ions inside the UCNP and the FRET acceptors on its surface.

EXPERIMENTAL SECTION

Chemicals. $ErCl_3·6H_2O$ 99.9%, $YbCl_3·6H_2O$ 99.998%, $YCl_3·6H_2O$ 99.99%, oleic acid (OA) technical grade 90%, NH_4F 98%, NaOH 98%, methanol 99.9%, anhydrous *N*,*N*-dimethyl formamide 99.8%, 1-octadecene (1-ODE) technical grade 90%, *n*-hexane 97%, tetraethyl orthosilicate (TEOS) 98%, succinic anhydride 99%, NH_4OH ACS reagent 28−30%, IGEPAL CO-520, (3-aminopropyl)-triethoxysilane (APTES) 99%, and CdTe core-type QDs COOH functionalized (part number 777943) were acquired from Sigma-Aldrich and used as received.

Synthesis of $NaY_{0.78}F_4:Yb_{0.2},Er_{0.02}$. The synthesis of monodisperse UCNPs with a composition of $NaY_{0.78}F_4:Yb_{0.2},Er_{0.02}$ was performed by using the oleate route, which was first reported by Li and Zhang.[27] Briefly, 15 mL of 1-ODE and 6 mL of OA were mixed in a 100 mL round bottom flask with three necks. $YCl_3·6H_2O$ (233 mg; 0.78 mmol), 78 mg of $YbCl_3·6H_2O$ (0.2 mmol), and 7.9 mg of $ErCl_3·6H_2O$ (0.02 mmol) were mixed with the previous solution and heated up at 140 °C for 1 h under a constant magnetic stirring and N_2 flow to ensure the complete dissolution of the rare earths and obtain a transparent solution with a yellowish color. After this time, the solution is cooled down at room temperature and a fresh methanol solution is prepared by dissolving 100 mg of NaOH (2.5 mmol) and 148 mg of NH_4F (4 mmol). The methanol solution with NaOH and NH_4F is added dropwise to the rare earth solution and left stirring for 30 min at room temperature. Finally, the temperature is raised at 110 °C with a constant N_2 flow, kept for 15 min at this temperature and for other 10 min under vacuum to ensure the complete evaporation of methanol and water. The temperature of the resulting solution is then raised to 330 °C and kept at this temperature for 60 min. After this time, the reaction was quickly cooled down to room temperature. The UCNPs were separated by centrifugation: we split the product in four different centrifuge tubes and filled them with a solution 1/1 of H_2O and ethanol. Then, we centrifuged the tubes at 8000 rpm for 10 min. The supernatant was discarded and the nanoparticles were resuspended in 0.5 mL of *n*-hexane and then reprecipitated with ethanol and centrifuged again at 8000 rpm for 10 min. Finally the UCNPs were resuspended in 10 mL of *n*-hexane with a concentration of 12 g/L and stored for further experiments.

Preparation of $NaY_{0.78}F_4:Yb_{0.2},Er_{0.02}@SiO_2−NH_2$. The UCNPs were covered with different thicknesses of SiO_2, following the reverse microemulsion method.[28,29] IGEPAL CO-520 (240 μL) were mixed with 4 mL of *n*-hexane, 1 mL of UCNPs dispersed in the previous solution (12 g/L), and 40 μL of NH_4OH. The resulting solution was submitted to sonication until a transparent emulsion was formed. Different volumes of TEOS ranging from 10 to 30 μL were added depending on the desired SiO_2 shell thickness. The reaction was stopped after 18 h with the addition of methanol to disrupt the microemulsion, and then, it was centrifuged at 9000 rpm for 10 min, and the supernatant was discarded. This process was repeated three times to remove the excess of IGEPAL CO-520. Finally, the SiO_2 surface was functionalized with the amino groups by the addition of APTES (15 μL, 0.068 mmol) to the synthesized UCNPs@SiO_2 dispersed in 5 mL of ethanol. The heterogeneous solution was stirred overnight at room temperature, and the next day, the UCNPs@$SiO_2−NH_2$ were recovered by centrifugation at 9000 rpm for 10 min. The supernatant was discarded and the nanoparticles were redispersed in ethanol. This process was repeated three times.

Morphological Characterization. Transmission electron microscopy (TEM) images were acquired using a JEOL JEM 1010 microscope operated at 80 kV (JEOL, Japan; 80 kV) equipped with a digital camera Gatan MegaView II. High-resolution TEM (HRTEM) and low-angle annular dark field scanning TEM images were acquired using a JEOL JEM 3000F operated at 300 kV and a Gatan ADF detector.

Optical Characterization. Absorbance spectra of QDs water solutions at different concentrations were measured using a UV−vis spectrometer (Ocean Optics, Red Tide 650) with 3 mm path length cuvettes.

Upconversion luminescence spectra were recorded with a fluorescence home-built system. The excitation beam comes from a pigtailed 10 W CW laser (JDSU, L4-9897603) working at 976 nm and provided with a current and temperature controller (ILX Lightwave, LDX-36025-12 and LDT-5525B, respectively). The laser beam is transmitted through a long-pass dichroic filter

DOI: 10.1021/acs.jpcc.8b04908
J. Phys. Chem. C 2018, 122, 18751−18758

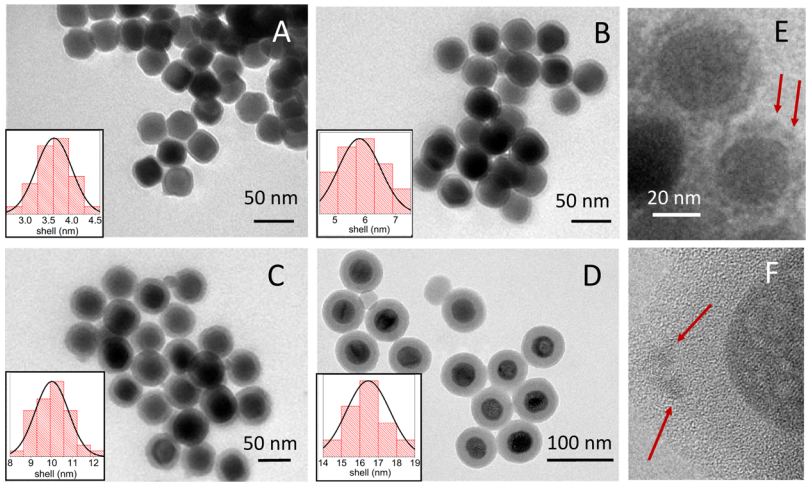

Figure 1. TEM micrographs of the synthesized $NaYF_4$:Yb,Er@SiO_2 nanoparticles with different SiO_2 shell thicknesses: (A) (3.6 ± 0.4), (B) (5.8 ± 0.7), (C) (10.0 ± 0.8), and (D) (16 ± 1) nm. (E) TEM and (F) HRTEM micrographs after attaching CdTe QDs (marked with arrows) on the surface of the $NaYF_4$:Yb,Er@SiO_2 nanoparticles.

(Semrock, FF757-Di01) and then focused on the sample with a 10× objective. The upconversion photoluminescence coming from the sample is reflected by the dichroic mirror toward a short-pass filter which blocks the IR reflected radiation (Semrock, FF01-775/SP). Then, it is focused into an optical fiber connected to a monochromator (HORIBA Jobin Yvon, iHR320). The monochromator is equipped with a photomultiplier tube (PMT) (HAMAMATSU, R928) and uses a 1200 g/mm grating blazed at 900 nm. To characterize the laser intensity in the sample, we measure the laser power with a thermal sensor power meter (Thorlabs, S310C) and the beam size using the slit scan technique.[30] The beam size (half width at half-maximum) is around 150 μm. In our measurements, we use excitation laser powers around 1.5 W, leading to laser intensities around 2 kW/cm^2. This allows us to ensure that the laser operates below the excitation saturation intensity of the transition $^2F_{7/2} \rightarrow {}^2F_{5/2}$ for the Yb^{3+} ions (see Figure 2B), which is $I_{sat} = \hbar\omega/(2\sigma\tau_{Yb}) = 3$ kW/cm^2, where $\tau_{Yb} = 2$ ms is the excited level lifetime, and $\sigma = 1.7 \times 10^{-20}$ cm^2 is the absorption cross-section.

Upconversion Emission Lifetime Measurements. Luminescence lifetimes were measured using the time-resolved photon counting method. Laser current is pulsed to generate excitation pulses of 40 μs with a repetition rate of 125 Hz. The luminescence emission at 540 nm is detected by the PMT, which is directly connected (without using a pre-amplifier) to a 50 Ω input of a digital oscilloscope (Agilent, DSO9104A). The signal from the laser current controller is used to trigger the oscilloscope. We developed a MATLAB program that analyzes directly in the oscilloscope each recorded signal in real-time. This code simulates the discriminator and the multichannel counter.[31] Upon analysis of more than 5000 trigger signals, we obtain a luminescence decay curve. Decay curve measurements were repeated at least three times for each sample under the same experimental conditions.

RESULTS AND DISCUSSION

To study the distance dependence of energy transfer between UCNP and QD pairs, we covered the surface of the UCNPs with a controlled thickness, uniform, amorphous silica layer. TEM micrographs from the as-synthesized UCNPs@SiO_2−NH_2 show highly monodisperse UCNPs with a mean diameter of (33 ± 3) nm (see Figure 1). We varied the SiO_2 shell thickness from 3 to 16 nm. As an example, Figure 1 shows TEM images for UCNPs@SiO_2−NH_2 with different silica shell thicknesses: (A) 3.6, (B) 5.8, (C) 10, and (D) 16 nm. After surface modification with amine groups, the $NaYF_4$:Yb,Er@SiO_2−NH_2 nanoparticles have a z-potential of +22 mV. CdTe QDs have an average diameter of 3 nm. QDs are functionalized with carboxylic groups and have a z-potential of −27 mV, so strong electrostatic interaction between positively charged UCNPs and negatively charged QDs will occur.

We prepared a solution containing UCNPs@SiO_2−NH_2 and CdTe−COOH QDs. First, the UCNPs@SiO_2−NH_2 were dispersed in ethanol at 5 g/L (1×10^{-7} M), while the CdTe−COOH QDs were dispersed in distilled water at 2.5 g/L (5×10^{-5} M). Then, we mixed equal volumes of the ethanol solution with the UCNPs@SiO_2−NH_2 and the aqueous solution with the CdTe−COOH QDs, so that an excess of QDs was used (QDs−UCNPs ratio of 478). A similar ratio has been used by Marin et al.[26] Negatively charged QDs were electrostatically adsorbed on the surface of positively charged UCNPs, as shown in the TEM and HRTEM images of Figure 1E,F, respectively. Single drops of this mixture were placed on a filter paper and allowed to dry at room temperature in air. The filter paper containing the mixture was set between two microscope glass slides for optical characterization.

As a reference, in the same way we prepared a filter paper with a drop of the ethanol solution containing UCNPs@SiO_2−NH_2 and distilled water without QDs mixed in equal volumes (hereafter named series I). In this reference sample, we use the same UCNP concentration than that of the sample with both UCNPs and QDs, while avoiding possible changes in the contributions to luminescence quenching due to water.[5] In a second experiment (hereafter, referred to as series II), the reference sample is made by using only the ethanol solution containing UCNPs@SiO_2−NH_2. In this last case, the possible effect of water was accounted for by taking into consideration that energy transfer between UCNPs and QDs should be negligible at very large UCNP−QD distances. This allows us to test the robustness of our experiments.

Figure 2A shows the optical characterization for the as-synthesized donors (UCNPs) and the acceptors (QDs) used in the FRET system under consideration. The upconversion

DOI: 10.1021/acs.jpcc.8b04908
J. Phys. Chem. C 2018, 122, 18751−18758

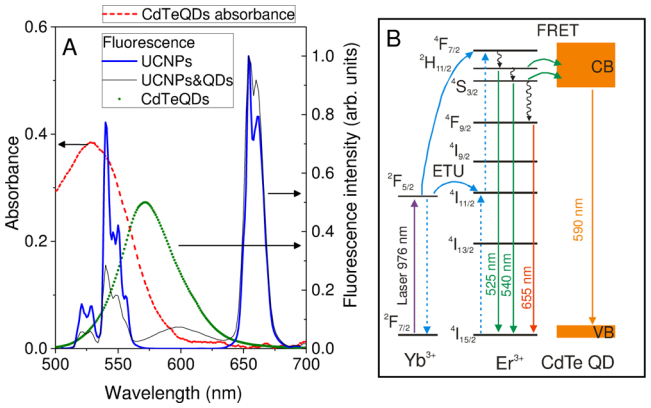

Figure 2. (A) (Left axis) Absorbance spectrum for 0.5 g/L water solution of CdTe QDs in a 3 mm cuvette (red curve). (Right axis) Fluorescence spectrum for: CdTe QDs water solution when excited at 455 nm (green curve), UCNPs@SiO_2 ethanol solution when excited at 976 nm (blue curve), and UCNPs@SiO_2 (3 nm-shell) with QDs dry sample when excited at 976 nm (black curve). (B) ETU scheme for populating the green emission levels $^2H_{11/2}$ and $^4S_{3/2}$ by a 976 nm laser and FRET scheme from these levels to the CdTe QD.

luminescence emission spectrum of $NaYF_4$:Yb,Er@SiO_2 nanoparticles under a 976 nm CW excitation laser is shown in Figure 2A (blue curve, right axis). Two green emission peaks near 525 and 540 nm are observed. These peaks correspond to $^2H_{11/2} \rightarrow {}^4I_{15/2}$ and $^4S_{3/2} \rightarrow {}^4I_{15/2}$ transitions of the Er^{3+} ions, respectively (see in Figure 2B, the energy transfer upconversion (ETU) mechanism populating these two levels). A red emission, with similar intensity, near 655 nm is also observed because of $^4F_{9/2} \rightarrow {}^4I_{15/2}$ transition (see Figure 2B). Figure 2A also shows the absorbance of a CdTe QDs water solution with 0.5 g/L in a 3 mm path length cuvette (red curve, left axis). Notice that the size of the QDs can be inferred from the position of their absorption peak.[32,33] In our case, we found an absorption peak around 529 nm, that gives us an estimation of the QDs size of 3 nm, in good agreement with that obtained from HRTEM images. Therefore, because the green emission bands of the UCNPs (donors) perfectly overlap with the absorption peak of the QDs (acceptors), the possibility of an efficient nonradiative energy transfer from UCNPs to QDs is ensured provided that both are close enough. Additionally, the QDs fluorescence emission spectrum under excitation by a LED radiation at 455 nm is shown in Figure 2A (green curve, right axis). The QDs orange emission band whose peak is around 572 nm does not overlap with the emission bands of the Er^{3+} ions avoiding mixed fluorescent emissions.

Now, let us test the interaction between UCNPs and QDs. Figure 2A shows the luminescence emission spectrum from the dry sample containing UCNPs with QDs electrostatically adsorbed on their surface (black curve, right axis). There, a new emission peak around 600 nm and a reduction of the green emission bands of the UCNPs are observed. Both features reveal that QDs are being excited by the $^4S_{3/2}$, $^2H_{11/2} \rightarrow {}^4I_{15/2}$ transitions of the Er^{3+} ions. Note that QDs cannot be excited with the IR radiation that excites the UCNPs. The emission peak arising from the QDs fluorescence appears as red-shifted respect to that obtained for the QDs solution excited under UV light. This is due to the inner filter effect that becomes relevant when increasing the QDs concentration during the drying process (see Figure S1). A similar shift was previously reported in UCNP−QD dried samples.[23]

Because the reduction of the UCNPs green luminescence intensity is due to both nonresonant energy transfer and reabsorption, to characterize in detail the Er^{3+} to QD FRET mechanism, luminescence lifetime studies are needed. Thus, luminescence decay signals for Er^{3+} ions at 540 nm ($^4S_{3/2} \rightarrow {}^4I_{15/2}$) were measured. As an example, Figure 3 shows the

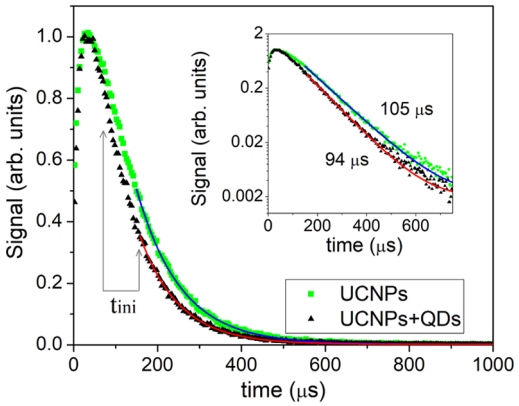

Figure 3. Normalized luminescence decay curves at 540 nm (transition $^4S_{3/2} \rightarrow {}^4I_{15/2}$) in the presence (black) or absence (green, series I) of CdTe QDs for UCNPs with a SiO_2 shell of 3 nm. Excitation laser at 976 nm with 40 μs pulses at 125 Hz. The arrows indicate the time range where the initial fitting time, t_{ini}, is varied. We set t_{final} = 1.2 ms. Inset: zoom of previous curves in a semilog scale.

luminescence intensity decay of UCNPs with a 3 nm silica shell, in the presence (black) and absence (green) of QDs. Fluorescence signals show an initial increase that is a signature of the upconversion process energy transfer from Yb^{3+} to Er^{3+} ions within the UCNPs, followed by an exponential decay. The luminescence decay time was obtained by fitting the decay curve to a single exponential function. For the fitting, we considered a time window from t_{ini} to t_{final}, where the final fitting time was set to t_{final} = 1.2 ms. For each experimental decay curve, we calculated around 25 fits by changing the initial fitting time t_{ini} within the range where the luminescence intensity varies from 70 to 30% of its maximum value. This fitting procedure gives us an average lifetime with its standard error. For the particular curve shown in Figure 3, the presence of the QDs reduces the luminescence lifetime from 104.7 ± 0.3 to 93.7 ± 0.2 μs. This decrease confirms the occurrence of nonradiative energy transfer from UCNPs to QDs. We have also corroborated that this energy transfer process produces a slow component (<100 μs) in the decay of the QD fluorescence at 590 nm, which otherwise would typically be in the nanosecond range (see the example in Figure S2 upper panel).

Once the FRET mechanism has been verified, its characterization is in order. FRET efficiency (E) can be computed from the experimental luminescence decay curves (as the ones shown in Figure 3) as

$$E = 1 - \frac{\tau_{DA}}{\tau_D} \quad (1)$$

where τ_D and τ_{DA} are the donor excited-state lifetime in the absence and in the presence of acceptor, respectively. For the particular case shown in Figure 3, an efficiency of E = (10.5 ± 0.4)% was achieved with a SiO_2 shell of 3 nm, which is quite high considering the relatively large diameter of the UCNPs (33 nm). Note that while luminescence emission comes from the Er^{3+} ions

DOI: 10.1021/acs.jpcc.8b04908
J. Phys. Chem. C 2018, 122, 18751−18758

distributed within the entire nanoparticle, ions far from the particle surface cannot participate in FRET.[22]

To analyze the behavior of FRET with the distance between the UCNPs and the QDs, we measured the luminescence decay times of UCNPs with different SiO_2 shell thicknesses, with and without QDs. The FRET efficiency as a function of shell thickness is plotted in Figure 4. The general trend is a fast

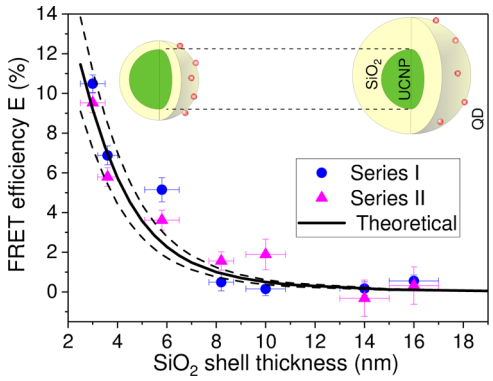

Figure 4. FRET efficiency, E, (eq 1) for different silica shell thicknesses on UCNPs with a diameter of 33 nm. Laser intensity: 1.7 kW/cm^2 (triangles), 2.4 kW/cm^2 (circles). Theoretical prediction of FRET efficiency (eq 7) for a Förster distance of R_0 = 5.5 nm and a number of QDs of 24 (solid line). Dashed lines correspond to the theoretical prediction under a variation of ±6 QDs.

decrease of the FRET efficiency for DA distances up to 12 nm, above which the energy transfer is negligible. A maximum FRET efficiency of around 10% is obtained, in agreement with the values reported in previous works.[23] We obtained similar results for the range of excitation laser intensities used in the experiments and also for the two reference samples, series I and II. Details on the method followed to take into account the water effect in series II are briefly described in the Supporting Information (see Table S1). The FRET efficiency curve calculated by measuring the luminescence decay signals at the QD emission channel, 590 nm, behaves as the one shown in Figure 4 (see Figure S2 lower panel).

Notice that our measurements do not show saturation of E as the silica shell thickness decreases, as it would be the case when dealing with a single DA pair. This feature is directly related to the fact of having a distribution of multiple donors (Er^{3+} ions) inside the UCNP as we will see later. Therefore, an estimation of the Förster radius R_0 from the experimental FRET efficiency curve cannot directly be obtained.

Theoretical FRET Efficiency. After analyzing the experimental data, let us now have a look at the theoretical counterpart for further interpretation of our results. The rate of energy transfer from a single donor to a single acceptor separated by a distance R is given by[2]

$$k_{ET} = \frac{9(\ln 10)}{128\pi^5 N_A n^4}\frac{\eta_D \kappa^2}{\tau_D R^6} J,$$
$$J = \int_{\Delta\lambda} F_D(\lambda)\epsilon_A(\lambda)\lambda^4 \, d\lambda \quad (2)$$

where N_A is the Avogadro's number, n is the refraction index of the medium surrounding the FRET pair, τ_D is the donor excited-state lifetime, and η_D is the intrinsic quantum yield of the donor in the absence of acceptor, that is, the quantum yield of the Er^{3+} ion excited state.[25] Note that $\eta_D = \tau_D/\tau_D^{rad}$, being τ_D^{rad} the radiative donor lifetime. Furthermore, κ^2 is a factor describing the relative orientation of the donor and the acceptor dipole moments, and the integral J measures the overlap between the donor emission spectrum and the acceptor absorption spectrum within the selected spectral donor emission region $\Delta\lambda$. Last, $F_D(\lambda)$ is the luminescence intensity of the donor normalized to the total intensity (i.e., $\int_{\Delta\lambda} F_D(\lambda)\, d\lambda = 1$), and $\epsilon_A(\lambda)$ is the molar extinction coefficient of the acceptor. In addition, the rate of energy transfer can be rewritten as

$$k_{ET} = \frac{1}{\tau_D}\left(\frac{R_0}{R}\right)^6 \quad (3)$$

where R_0 is the Förster distance defined as the distance at which half of the donor ions decay by transferring their energy to the acceptors, that is, the distance at which the energy transfer rate is equal to the donor decay rate in the absence of acceptor. By comparing eqs 2 and 3, one can obtain a closed expression for R_0 as follows

$$R_0 = 0.0211(\kappa^2 \eta_D n^{-4} J)^{1/6} \text{ [nm]} \quad (4)$$

where J is evaluated with the wavelength expressed in [nm] and the molar extinction coefficient in [M^{-1} cm^{-1}].

To estimate the Förster distance R_0, we calculate the overlap integral J from the experimental measurements of $\epsilon_A(\lambda)$ and $F_D(\lambda)$. The molar extinction coefficient of the QDs is obtained through the Beer–Lambert's law by measuring the absorbance at different concentrations and taking into account the cuvette path length (L = 3 mm). The result is shown in Figure 5. From

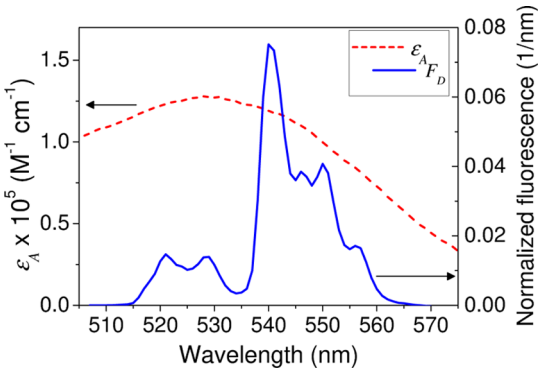

Figure 5. (Left axis) Molar extinction coefficient, $\epsilon_A(\lambda)$, of a 10^{-5} M QDs water solution in a cuvette with 3 mm path length. (Right axis) Upconversion luminescence intensity spectrum, $F_D(\lambda)$, (area under the curve in the green band region is normalized to unity) used to calculate the overlap integral J. Both represented as a function of the excitation wavelength λ.

the experimental data shown in Figure 5, the overlap integral results to be $J = 9.6 \times 10^{15}$ M^{-1} cm^{-1} nm^4. Note that this value can be roughly estimated by considering a nearly constant value of ϵ_A in the green region of the spectrum around $\lambda \simeq 540$ nm, which gives $J \simeq \epsilon_A \lambda^4 \simeq 10^{16}$ M^{-1} cm^{-1} nm^4.

Other important parameters necessary to evaluate eq 4 are κ, n, and η_D. The orientation factor of DA dipoles κ^2, is usually assumed to be 2/3; which corresponds to the dynamic random averaging. The material through which FRET mainly takes place is silica whose index of refraction is n = 1.46. Finally, the intrinsic quantum yield η_D, which measures the probability that donor de-excites radiatively in the absence of acceptor, has been estimated as around 20–30% by Bhuckory et al. from FRET measure-

DOI: 10.1021/acs.jpcc.8b04908
J. Phys. Chem. C 2018, 122, 18751–18758

ments of UCNPs with different core/shell architectures.[25] Note that this value is much larger than the one corresponding to the overall UCNP quantum yield. We estimate the intrinsic quantum yield by considering that the radiative lifetime for the excited-donor level ($^4S_{3/2}$) is in the millisecond range,[34] τ_D^{rad} = 0.5 ms and by using our experimental luminescence decay rate $\tau_D \simeq 105\ \mu s$. This leads to $\eta_D = \tau_D/\tau_D^{rad} \simeq 0.21$. For the sake of simplicity, we assume the quantum yield to be the same for all the UCNPs@SiO_2. This is reasonable because the donor lifetime obtained without QDs was quite similar throughout the range of silica shell thicknesses used in our experiments. Finally, by evaluating eq 4 with these parameters, our theoretical prediction for the Förster distance is $R_0 \simeq 5.5$ nm.

With this estimation in mind, to understand the observed dependency of the FRET efficiency on distance, we must consider the distribution of multiple DA pairs. First, let us express the transfer efficiency (i.e., the probability of de-excitation via energy transfer) of a single DA pair as

$$E_{Er-QD} = \frac{k_{ET}^{DA}}{1/\tau_D + k_{ET}^{DA}} = \frac{1}{1 + (R/R_0)^6} \quad (5)$$

From eq 5, we see how an Er^{3+} ion close to the UCNP external surface is able to transfer its energy to the QD for small silica shell thicknesses ($R < R_0$), whereas an ion close to the UCNP center will not be able to transfer its energy to the QD even in the absence of silica shell ($R > R_0$) (see Figure S3).

We consider that the energy transfer rate from each Er^{3+} ion inside the UCNP to all the QDs adsorbed onto its surface results from the sum of the single pair transfer rates: $k_{ET}^{D} = \sum_{A=1}^{N_{QD}} k_{ET}^{DA}(A)$, where N_{QD} is the total number of QD acceptors adsorbed onto the UCNP surface. Therefore, the FRET efficiency for each single Er^{3+} ion is

$$E_{Er-QDs} = \frac{\sum_{A=1}^{N_{QD}} k_{ET}^{DA}(A)}{1/\tau_D + \sum_{A=1}^{N_{QD}} k_{ET}^{DA}(A)} \quad (6)$$

Here, $k_{ET}^{DA}(A)$ results from the evaluation of eq 3 at the particular DA distance R for every case. Although we take N_{QD} as a fitting parameter in our simulations, we can roughly estimate this value from the TEM images as $N_{QD} \approx 20$. FRET efficiency is then calculated by averaging the efficiency of each Er^{3+} ion inside the nanoparticle

$$E = \langle E_{Er-QDs} \rangle_{N_{Er}} \quad (7)$$

Here, the number of Er^{3+} ions inside the nanoparticle is $N_{Er} = f_{Er} m_{NP} N_A / W = 4405$, where $f_{Er} = 0.019$ is the fraction of Er^{+3} ions, $W = 205.3$ g/mol is the molar weight of $NaYF_4$:Yb/Er, and $m_{NP} = 7.9 \times 10^{-17}$ g is the mass of the UCNP.

In our calculations, we generate a uniform random distribution of the Er^{3+} ions inside the UCNP,[35] and we compute the average FRET efficiency using eq 7 with the Förster distance calculated above, that is $R_0 = 5.5$ nm, and a number of QDs around the particle of 24. Our simulations result presented in Figure 4 (solid line) shows a very good agreement with the experimental data. We have also included in Figure 4 (dashed lines) theoretical curves with a different number of QDs, to account for the observed variation of the number of acceptors per UCNP in TEM images.

We conclude that the averaging process carried out when considering multiple DA configuration is needed to explain the FRET efficiency found in the experiments. For further analysis of this phenomenon, Figure 6 shows the distribution of FRET efficiency for each Er^{3+} ion, E_{Er-QDs}, as a function of its radial distance to the particle center (blue points). Significant energy transfer, larger than 10%, occurs only for those ions placed farther than 11 nm from the UCNP center. This means that only the ions in close proximity to the UCNP external surface (≤5.5 nm) are susceptible to efficiently transfer their energy to the QDs. However, we observe a wide distribution on FRET efficiencies even for these superficial ions because the QDs are randomly distributed on the silica shell without completely covering the UCNP surface (see the inset in Figure 6).

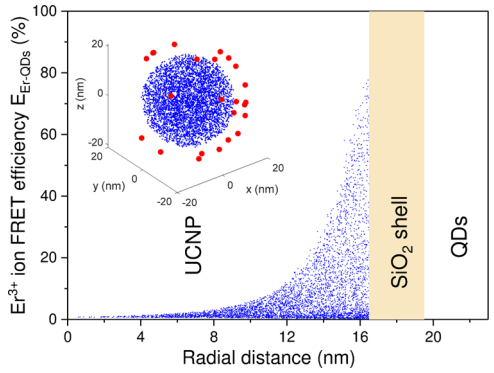

Figure 6. Distribution of the FRET efficiency achieved by each Er^{3+} ion inside an UCNP with 3 nm SiO_2 shell, E_{Er-QDs} (eq 6), as a function of the radial distance from the particle center. Inset: Distribution of Er^{3+} ions (blue points) inside a 33 nm UCNP with a SiO_2 shell of 3 nm and 24 QDs randomly adsorbed onto the particle-shell surface (red points).

Optimal Design of UCNPs for FRET Performance. As we mentioned in the Introduction, two different strategies have been used to increase the FRET efficiency in UCNP systems: reducing the UCNP size and developing inert-core/active-shell UCNP architectures.[25,26] In both cases, the fraction of active ions that can exhibit an efficient energy transfer increases. Marin et al.[26] have experimentally reported a two-fold FRET efficiency increase by applying these strategies to square-based bipyramidal shape UCNPs and QDs.

Let us use our theoretical approach to estimate the FRET efficiency that could be achieved under these two enhancement strategies for our particular UCNP−QD system. We consider UCNPs as the ones used in the experiments but with a tunable size inert-core, that is, particles with 33 nm of diameter, a silica shell of 3 nm, and we consider 24 QDs adsorbed onto the particle surface (see the particle scheme in Figure 7A). The quantum yield of particles with different inert-core diameters is expected to change. However, determining this magnitude is a challenging experimental problem, and as a first approximation, we consider here that all particles have roughly the same quantum yield, that is, the same Förster distance $R_0 = 5.5$ nm. Figure 7A shows the FRET efficiency and the number of Er^{3+} ions per nanoparticle as a function of the inert-core radius. We observe that to obtain a notable increase of FRET efficiency, an inert-core radius larger than half of the particle radius is required (see blue symbols in Figure 7A, left axis). Note that the reduction in the total number of Er^{3+} ions in a particle with an inert core is not significant until the inert core takes half of the particle radius (see black symbols in Figure 7A, right axis). We obtain a two-fold FRET efficiency increase when the inert radius is almost as large as the particle radius, that is, when the active shell is around 2 nm thick.

Finally, we now analyze the effect of the UCNP size on the FRET response. We consider UCNPs with diameter from 32 to

DOI: 10.1021/acs.jpcc.8b04908
J. Phys. Chem. C 2018, 122, 18751−18758

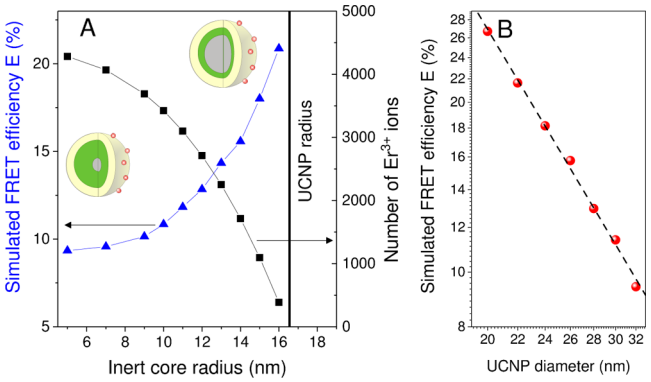

Figure 7. (A) Simulated FRET efficiency, E, from eq 7, (left axis) and total number of Er^{3+} ions inside each UCNP, N_{Er}, (right axis) as a function of the inert core radius for a particle with a diameter of 33 nm. (B) Simulated FRET efficiency, E, from eq 7, as a function of the UCNP diameter d_{NP} (symbols). The dashed line is the linear fit in the log−log plot.

20 nm, all particles with a 3 nm silica shell. The number of QDs adsorbed onto the UCNP surface and the donor quantum yield are properties that depend on the UCNP size; however, for the sake of simplicity, we consider the values previously used, that is, $N_{QD} = 24$ and $R_0 = 5.5$ nm. Figure 7B shows the FRET efficiency as a function of the UCNP size in a log−log plot. The linear fit shown in this figure (dashed line) indicates that the FRET efficiency follows a power law behavior with the UCNP diameter d_{NP} with an exponent close to minus 2, that is, $E \propto d_{NP}^{-2}$. Under these assumptions, the change of FRET efficiency is proportional to the nanoparticle area. For example, by reducing the UCNP diameter from 33 to 23 nm, therefore reducing the nanoparticle volume by 1/3, we calculate a FRET efficiency of around 20%, which is similar to our previously calculated efficiency for a 33 nm particle consisting of a 2 nm active-shell and a 31 nm inert-core and doubles the value measured in our experiments for the 33 nm diameter UCNPs. Similar increases in efficiency with reductions in the particle diameter have been experimentally reported in a previous work.[26]

CONCLUSIONS

We have studied the FRET phenomenon from UCNPs to QDs, which is a system with several advantages. The CdTe QDs exhibit a strong absorption band that perfectly overlaps with the luminescence emission band of the UCNPs. Furthermore, cross-excitation is avoided because the IR UCNP donor excitation does not produce fluorescence in the QD acceptors. We experimentally verified FRET between 33 nm diameter positively charged $NaYF_4$:Yb,Er@SiO_2−NH_2 particle donors and 3 nm diameter negatively charged CdTe−COOH QDs acceptors. In our system, several small CdTe QDs were adsorbed on each larger UCNP@SiO_2 surface by electrostatic interaction. This multiple acceptor configuration enhances the FRET response. The QD adsorption leads to a significant reduction of the upconversion luminescence lifetime, which clearly demonstrates that an additional decay pathway for the excited UCNPs takes place because of non-radiative energy transfer to the QDs. FRET is limited by the fact that the donor and acceptor must be in extreme close proximity. Considering the overlap between the donor emission spectrum and the acceptor absorption spectrum, we calculated a value for the Förster distance of $R_0 \simeq 5.5$ nm, assuming an intrinsic quantum yield of the Er^{3+} ions in the excited level $^4S_{3/2}$ of 0.21. This is a large value compared to the Förster radius characteristic of organic fluorophores of a few angstroms to 2 nm, but still small compared to the UCNP radius. We experimentally analyzed the effect of the UCNP−QD distance in the FRET efficiency by varying the thickness of the UCNPs silica shell from 3 to 16 nm. A maximum FRET efficiency of around 10% is achieved for the 3 nm silica shell, which is a remarkably large value if we take into account the distribution of all the potential donors, that is, Er^{3+} ions, inside the relatively large UCNP in comparison with the Förster distance. The UCNP-to-QD nonradiative interaction vanishes for distances above 12 nm.

We have theoretically explained the experimental results by calculating the FRET efficiency of each single Er^{3+} ion−QD pair and averaging the FRET response of every Er^{3+} ion inside the UCNP. Therefore, to theoretically obtain accurate values of the FRET efficiency in UCNP-based FRET systems, this averaging process is required. Indeed, we were able to establish that only Er^{3+} ions placed in close proximity to the UCNP surface, in a shell of around 5 nm (similar to the Förster distance), are able to participate in an energy transfer process with $E > 10\%$.

In summary, our work supports that the main physical characteristics governing the UCNP-to-QD energy transfer process is the relative spatial configuration of donors and acceptors. Our results show that the as-proposed UCNP−QD FRET system is a good potential platform for biosensing short biomolecules whose length of interaction is below the estimated Förster distance (≤6 nm). Nanoparticle systems with alternative architectures, as the ones discussed in this work, can be used to improve the distribution of DA distances for more efficient FRET-based biosensing applications.

ASSOCIATED CONTENT

Supporting Information

The Supporting Information is available free of charge on the ACS Publications website at DOI: 10.1021/acs.jpcc.8b04908.

Fluorescence spectrum of CdTe QDs excited at 455 nm: water solution and dried sample; FRET analysis at the acceptor QDs emission channel (590 nm); experimental FRET efficiency calculation from lifetimes; and theoretical FRET efficiency of a single Er^{3+} ion to a single QD (PDF)

AUTHOR INFORMATION

Corresponding Authors

*E-mail: smelle@fis.ucm.es (S.M.).
*E-mail: bjrubio@ucm.es (J.R.-R.).

ORCID

Sonia Melle: 0000-0002-9802-6908
Marco Laurenti: 0000-0002-0273-7423
Jorge Rubio-Retama: 0000-0002-1785-5844

Notes

The authors declare no competing financial interest.

ACKNOWLEDGMENTS

This work was supported by Universidad Complutense de Madrid and Santander Bank (PR26/16-12B), Ministerio de Economía y Competitividad-MINECO (MAT2016-75955, MAT2017-83111R), The European Upconversion Network COST Action CM1403 (2014-2018), and Comunidad de Madrid (B2017/BMD-3867 RENIM-CM) co-financed by European Structural and Investment Fund. D.M.-G. thanks

DOI: 10.1021/acs.jpcc.8b04908
J. Phys. Chem. C 2018, 122, 18751−18758

UCM-Santander for a predoctoral contract (CT17/17-CT18/17). TEM images were obtained at the National Center for Electron Microscopy (UCM, Madrid) facility.

REFERENCES

(1) Förster, T. Zwischenmolekulare Energiewanderung und Fluoreszenz. *Ann. Phys.* **1948**, *437*, 55−75.
(2) Lakowicz, J. R. *Principles of Fluorescence Spectroscopy*, 3rd ed.; Springer: New York, USA, 2006.
(3) Stryer, L.; Haugland, R. P. Energy Transfer: A Spectroscopic Ruler. *Proc. Natl. Acad. Sci. U.S.A.* **1967**, *58*, 719−726.
(4) Byrne, A. G.; Byrne, M. M., III; Gemmill, K. B.; Spillmann, C.; Medintz, I.; Sloan, S. L.; van der Meer, B. W. *FRET Förster Resonance Energy Transfer*; Wiley-Blackwell, 2013; Chapter 14, pp 655−755.
(5) Riuttamäki, T.; Hyppänen, I.; Kankare, J.; Soukka, T. Decrease in Luminescence Lifetime Indicating Nonradiative Energy Transfer from Upconverting Phosphors to Fluorescent Acceptors in Aqueous Suspensions. *J. Phys. Chem. C* **2011**, *115*, 17736−17742.
(6) Vetrone, F.; Naccache, R.; Morgan, C. G.; Capobianco, J. A. Luminescence Resonance Energy Transfer from an Upconverting Nanoparticle to a Fluorescent Phycobiliprotein. *Nanoscale* **2010**, *2*, 1185−1189.
(7) Kuningas, K.; Päkkilä, H.; Ukonaho, T.; Rantanen, T.; Lövgren, T.; Soukka, T. Upconversion Fluorescence Enables Homogeneous Immunoassay in Whole Blood. *Clin. Chem.* **2007**, *53*, 145−146.
(8) Jiang, S.; Zhang, Y. Upconversion Nanoparticle-Based FRET System for Study of siRNA in Live Cells. *Langmuir* **2010**, *26*, 6689−6694.
(9) Chen, N.-T.; Cheng, S.-H.; Liu, C.-P.; Souris, J.; Chen, C.-T.; Mou, C.-Y.; Lo, L.-W. Recent Advances in Nanoparticle-Based Förster Resonance Energy Transfer for Biosensing, Molecular Imaging and Drug Release Profiling. *Int. J. Mol. Sci.* **2012**, *13*, 16598−16623.
(10) Ding, Y.; Wu, F.; Zhang, Y.; Liu, X.; de Jong, E. M. L. D.; Gregorkiewicz, T.; Hong, X.; Liu, Y.; Aalders, M. C. G.; Buma, W. J.; et al. Interplay between Static and Dynamic Energy Transfer in Biofunctional Upconversion Nanoplatforms. *J. Phys. Chem. Lett.* **2015**, *6*, 2518−2523.
(11) Huang, Y.; Hemmer, E.; Rosei, F.; Vetrone, F. Multifunctional Liposome Nanocarriers Combining Upconverting Nanoparticles and Anticancer Drugs. *J. Phys. Chem. B* **2016**, *120*, 4992−5001.
(12) DaCosta, M. V.; Doughan, S.; Han, Y.; Krull, U. J. Lanthanide Upconversion Nanoparticles and Applications in Bioassays and Bioimaging: A Review. *Anal. Chim. Acta* **2014**, *832*, 1−33.
(13) Liu, J.; Liu, Y.; Bu, W.; Bu, J.; Sun, Y.; Du, J.; Shi, J. Ultrasensitive Nanosensors Based on Upconversion Nanoparticles for Selective Hypoxia Imaging in Vivo upon Near-Infrared Excitation. *J. Am. Chem. Soc.* **2014**, *136*, 9701−9709.
(14) Nyk, M.; Kumar, R.; Ohulchanskyy, T. Y.; Bergey, E. J.; Prasad, P. N. High Contrast in Vitro and in Vivo Photoluminescence Bioimaging Using Near Infrared to Near Infrared Up-Conversion in Tm3+and Yb3+Doped Fluoride Nanophosphors. *Nano Lett.* **2008**, *8*, 3834−3838.
(15) Zhou, J.; Liu, Z.; Li, F. Upconversion Nanophosphors for Small-Animal Imaging. *Chem. Soc. Rev.* **2012**, *41*, 1323−1349.
(16) Zwier, J. M.; Hildebrandt, N. In *Reviews in Fluorescence 2016*; Geddes, C. D., Ed.; Springer: Cham, 2016; pp 17−43.
(17) Mendez-Gonzalez, D.; Lopez-Cabarcos, E.; Rubio-Retama, J.; Laurenti, M. Sensors and Bioassays Powered by Upconverting Materials. *Adv. Colloid Interface Sci.* **2017**, *249*, 66−87.
(18) Charbonnière, L. J.; Hildebrandt, N.; Ziessel, R. F.; Löhmannsröben, H.-G. Lanthanides to Quantum Dots Resonance Energy Transfer in Time-Resolved Fluoro-Immunoassays and Luminescence Microscopy. *J. Am. Chem. Soc.* **2006**, *128*, 12800−12809.
(19) Doughan, S.; Han, Y.; Uddayasankar, U.; Krull, U. J. Solid-Phase Covalent Immobilization of Upconverting Nanoparticles for Biosensing by Luminescence Resonance Energy Transfer. *ACS Appl. Mater. Interfaces* **2014**, *6*, 14061−14068.
(20) Cui, S.; Xu, S.; Song, H.; Xu, W.; Chen, X.; Zhou, D.; Yin, Z.; Han, W. Highly Sensitive and Selective Detection of Mercury Ions Based on Up-conversion FRET from NaYF4:Yb3+/Er3+ Nanophosphors to CdTe Quantum Dots. *RSC Adv.* **2015**, *5*, 99099−99106.
(21) Hildebrandt, N.; Spillmann, C. M.; Algar, W. R.; Pons, T.; Stewart, M. H.; Oh, E.; Susumu, K.; Díaz, S. A.; Delehanty, J. B.; Medintz, I. L. Energy Transfer with Semiconductor Quantum Dot Bioconjugates: A Versatile Platform for Biosensing, Energy Harvesting, and Other Developing Applications. *Chem. Rev.* **2017**, *117*, 536−711.
(22) Mattsson, L.; Wegner, K. D.; Hildebrandt, N.; Soukka, T. Upconverting Nanoparticle to Quantum Dot FRET for Homogeneous Double-nano Biosensors. *RSC Adv.* **2015**, *5*, 13270−13277.
(23) Bednarkiewicz, A.; Nyk, M.; Samoc, M.; Strek, W. Up-conversion FRET from Er3+/Yb3+:NaYF4 Nanophosphor to CdSe Quantum Dots. *J. Phys. Chem. C* **2010**, *114*, 17535−17541.
(24) Muhr, V.; Würth, C.; Kraft, M.; Buchner, M.; Baeumner, A. J.; Resch-Genger, U.; Hirsch, T. Particle-Size-Dependent Förster Resonance Energy Transfer from Upconversion Nanoparticles to Organic Dyes. *Anal. Chem.* **2017**, *89*, 4868−4874.
(25) Bhuckory, S.; Hemmer, E.; Wu, Y.-T.; Yahia-Ammar, A.; Vetrone, F.; Hildebrandt, N. Core or Shell? Er3+ FRET Donors in Upconversion Nanoparticles. *Eur. J. Inorg. Chem.* **2017**, 5186.
(26) Marin, R.; Labrador-Paéz, L.; Skripka, A.; Haro-González, P.; Benayas, A.; Canton, P.; Jaque, D.; Vetrone, F. Upconverting Nanoparticle to Quantum Dot Förster Resonance Energy Transfer: Increasing the Efficiency through Donor Design. *ACS Photonics* **2018**, *5*, 2261−2270.
(27) Li, Z.; Zhang, Y. An Efficient and User-friendly Method for the Synthesis of Hexagonal-phase NaYF4:Yb, Er/Tm Nanocrystals with Controllable Shape and Upconversion Fluorescence. *Nanotechnology* **2008**, *19*, 345606.
(28) Alonso-Cristobal, P.; Lopez-Quintela, M. A.; Contreras-Caceres, R.; Lopez-Cabarcos, E.; Rubio-Retama, J.; Laurenti, M. Synthesis of Catalytically Active Gold Clusters on the Surface of Fe3O4@SiO2 Nanoparticles. *RSC Adv.* **2016**, *6*, 100614−100622.
(29) Zhelev, Z.; Ohba, H.; Bakalova, R. Single Quantum Dot-Micelles Coated with Silica Shell as Potentially Non-Cytotoxic Fluorescent Cell Tracers. *J. Am. Chem. Soc.* **2006**, *128*, 6324−6325.
(30) McCally, R. L. Measurement of Gaussian Beam Parameters. *Appl. Opt.* **1984**, *23*, 2227.
(31) Stacewicz, T.; Krainska-Miszczak, M. Time-resolved Photon Counting with Digital Oscilloscope. *Meas. Sci. Technol.* **1997**, *8*, 453−455.
(32) Yu, W. W.; Qu, L.; Guo, W.; Peng, X. Experimental Determination of the Extinction Coefficient of CdTe, CdSe, and CdS Nanocrystals. *Chem. Mater.* **2003**, *15*, 2854−2860.
(33) Dagtepe, P.; Chikan, V.; Jasinski, J.; Leppert, V. J. Quantized Growth of CdTe Quantum Dots; Observation of Magic-Sized CdTe Quantum Dots. *J. Phys. Chem. C* **2007**, *111*, 14977−14983.
(34) Weber, M. J. Radiative and Multiphonon Relaxation of Rare-Earth Ions inY2O3. *Phys. Rev.* **1968**, *171*, 283−291.
(35) Knuth, D. E. *The Art of Computer Programming, Vol. 2: Seminumerical Algorithms*, 3rd ed.; Addison-Wesley: Boston, USA, 1999.

DOI: 10.1021/acs.jpcc.8b04908
J. Phys. Chem. C 2018, 122, 18751−18758